

# High resolution in non-destructive testing: A review

Cite as: J. Appl. Phys. **132**, 100901 (2022); doi: [10.1063/5.0095328](https://doi.org/10.1063/5.0095328)

Submitted: 9 April 2022 · Accepted: 5 August 2022 ·

Published Online: 9 September 2022



Anish Kumar<sup>1,a)</sup> and Walter Arnold<sup>2,b)</sup>

## AFFILIATIONS

<sup>1</sup>Metallurgy and Materials Group, Indira Gandhi Centre for Atomic Research, A CI of Homi Bhabha National Institute, Kalpakkam 603102, Tamil Nadu, India

<sup>2</sup>Department of Material Science and Engineering, Saarland University, Campus E 2.6, 66123 Saarbrücken, Germany

**Note:** This paper is part of the Special Topic on Non-Invasive and Non-Destructive Methods and Applications Part II.

**a) Author to whom correspondence should be addressed:** [anish@igcar.gov.in](mailto:anish@igcar.gov.in)

**b)** [w.arnold@mx.uni-saarland.de](mailto:w.arnold@mx.uni-saarland.de)

## ABSTRACT

Since the beginning of the applications of non-destructive testing/evaluation (NDT/NDE) techniques, efforts have been made consistently to improve their detection sensitivity and resolution. In the present paper, factors governing lateral resolution in three major NDT techniques, viz., ultrasonic testing (UT), x-ray radiographic testing (XRT), and eddy current testing (ECT) are presented. Furthermore, a review of recent advances in these NDT techniques to reach the theoretically achievable resolution limit or even surpassing the same using alternate approaches is also discussed. For example, resolution in UT is theoretically limited to half the wavelength by the Rayleigh limit; however, subwavelength resolutions have been achieved through the applications of near field methods by capturing the evanescent field. On the other hand, the resolution achieved in XRT is primarily limited to half the source/focal spot size, which is many orders of magnitude larger than the wavelength. Over the years, the reduction in the focal spot from macro-focus to micro-focus and now to nano-focus has led to improvement in the resolution to a few nanometers, of course, in combination with suitable magnification required due to detectors with limited pixel size (a few  $\mu\text{m}$  to a few 10 s of  $\mu\text{m}$ ). Similarly, innovations in electromagnetic/magnetic sensors have significantly improved the resolution achieved in ECT. Atomic force microscopy, metamaterials, and artificial neural network-based methods have been employed for obtaining high-resolution NDE images. At the end, authors' perspective toward possible directions for high-resolution NDT is presented.

Published under an exclusive license by AIP Publishing. <https://doi.org/10.1063/5.0095328>

## I. INTRODUCTION

Every non-destructive testing/evaluation (NDT/NDE) technique has its own domain of applications, with a few techniques having a wider application range. Most of the research and development in the field of NDT have been essentially targeted toward improving one of the two parameters of the techniques, viz., (i) sensitivity and (ii) resolution. While sensitivity refers to the smallest feature that can be detected by an NDT technique, resolution refers to the ability to distinctly identify two closely spaced features as separate identities. Even though the two parameters provide two different characteristics of an NDT technique, material parameters affecting one normally affect the other too. For example, a material with larger ultrasonic scattering leads to reduced sensitivity and, thus, requires lower frequency to be used

for inspection at similar depths. This eventually deteriorates the resolution. Furthermore, reduced sensitivity may lead to a decrease in the signal-to-noise ratio (SNR), which also leads to deterioration in resolution. There are different types of resolution referred in NDT, such as lateral resolution, depth resolution, and contrast resolution. In the present paper, resolution refers essentially to lateral resolution, unless specifically mentioned otherwise.

Out of the various NDT techniques, ultrasonic testing (UT),<sup>1</sup> eddy current testing (ECT),<sup>2,3</sup> and x-ray radiographic testing (XRT)<sup>4</sup> are the three most widely used and researched NDT techniques due to their versatility and practical applicability in order to provide information about surface, subsurface, and volumetric (limited in ECT) discontinuities in a component. The resolution

achieved in different variants of these three techniques is discussed in the present paper. These three techniques also represent three different groups of techniques working on the principles of wave propagation (UT and microwave imaging), particle absorption and shadow projection (XRT,  $\gamma$ -ray, neutrons, etc.), and magnetic/electromagnetic interaction (ECT and magnetic techniques including magnetic flux technique). Table I provides key limiting factors in the three techniques for achieving high resolution. A few important techniques or approaches developed to circumvent the limitations are also listed in Table I and discussed in more details in Secs. II–IV.

One of the most important factors affecting resolution of an NDT technique is the depth of the defect or the thickness of the component. For the techniques requiring single side access such as ECT and UT, resolution is governed by the depth at which the defect is located in the component. The thickness of the component affects the resolution in XRT, which works in through the transmission mode. Figure 1 shows schematically the variations in spatial resolution achievable in different NDE techniques at different depths of a defect or for different object thicknesses. In general, it can be seen that the achievable lateral resolution depends on the depth of the defects for all the techniques. At a given depth of defect, the resolution achievable is also dependent upon the physical and microstructural properties of the material being tested. The details of the resolution achieved are discussed in subsequent sections separately for different techniques.

Sections II–IV of the paper present the physical basis of the factors limiting resolution in the three techniques, respectively, followed by a review of the possible methods for their improvement. Various possible ways for improvement in resolution in these NDT techniques from mm to nm range in the view of physical factors affecting the lateral resolution are presented by citing a few representing articles. The paper focuses on applications of the selected NDT techniques in materials science, applied physics, and engineering fields. Even though, the present paper does not specifically include medical applications of the NDT techniques, the basic physics and most of the approaches for improved resolution apply in the medical diagnostic field as well.

## II. ULTRASONIC TECHNIQUES

Lateral resolution achieved in UT is limited to half the wavelength by the classical Rayleigh criterion, similar to any other wave-based imaging technique.<sup>34</sup> Hence, an obvious choice for decreasing (improving) resolution is to increase the operating frequency. However, in most of the practical applications, the resolution limit achieved is much larger than the Rayleigh criterion due to other limiting factors. These factors limiting the lateral resolution in UT are discussed below first, followed by various means of improving resolution to reach the Rayleigh limit and then techniques surpassing this limit.

Another important parameter in UT is the depth resolution that indicates the ability of an ultrasonic inspection system to

**TABLE I.** Summary of the factors affecting resolution in ultrasonic testing (UT), eddy current testing (ECT) and x-ray radiographic testing (RT) techniques, proposed approaches/techniques for their improvement, and corresponding important references.

Techniques	References for basic principles	Limiting factors for resolution		Techniques/approaches for improving resolution
		Material related	Technique related	
Ultrasonic	Krautkrämer and Krautkrämer <sup>1</sup>	Grain scattering, <sup>5</sup> depth of defect <sup>1,6</sup>	Wavelength, <sup>1,6,7</sup> aperture <sup>1,6</sup>	Focused probe UT (FUT), <sup>8,9</sup> synthetic aperture focusing technique (SAFT), <sup>10,11</sup> phased array ultrasonic technique (PAUT), <sup>12</sup> scanning acoustic microscopy (SAM), <sup>13,14</sup> metamaterials (MM) based UT, <sup>15–17</sup> time reversal-multiple signal classification (TR-MUSIC), <sup>18</sup> atomic force acoustic microscopy (AFAM) <sup>19,20</sup>
X-ray Radiography	Halmshaw <sup>4</sup>	Component thickness, <sup>4</sup> density <sup>4</sup>	Source/anode size, detector pixel resolution, detector size, source to object and object to detector distance <sup>4</sup>	Micro-focal x-ray radiographic testing ( $\mu$ -XRT), <sup>21</sup> nano-focal XRT, <sup>22</sup> synchrotron-XRT (S-XRT), <sup>23</sup> S-XRT using Fresnel lenses (S-XRT-FL), <sup>24</sup> laser wake field accelerator-inverse Compton scattering (LWFA-ICS), <sup>25</sup> scanning coherence diffraction microscopy (SCDM) or ptychography <sup>26</sup>
Eddy current	Bowler, <sup>2</sup> Hagemier, <sup>3</sup> Dodd and Deed <sup>27</sup>	Depth of defect, conductivity, and permeability	Frequency, dimensions of the exciter coil, <sup>28</sup> and foot-print of the receiver	Focused ECT, <sup>29</sup> solid state sensors-based ECT (SSS-ECT), <sup>30</sup> eddy current microscopy (ECM) by reducing the foot-print of the probe, <sup>31</sup> eddy current-atomic force microscopy (EC-AFM) <sup>32</sup>

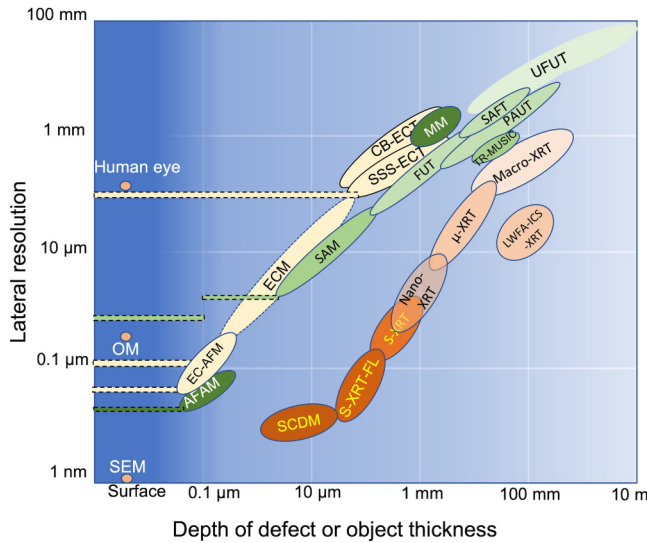


**FIG. 1.** Typical spatial resolution achievable in different NDE techniques at different defect depths (for single side access techniques such as ECT and UT) or for different object thicknesses (for XRT). These values are influenced by the test material and the typical range for steels is presented here. UFUT, un-focused UT using mono-element probes;<sup>1</sup> FUT, focused UT using mono-element probes;<sup>8,9</sup> SAFT, synthetic aperture focusing technique;<sup>10,11</sup> PAUT, phased array ultrasonic technique;<sup>12</sup> SAM, scanning acoustic microscope;<sup>13,14</sup> AFM, atomic force acoustic microscope;<sup>19,20</sup> MM, metamaterials-based UT;<sup>15–17</sup> TR-MUSIC, time reversal-multiple signal classification;<sup>18</sup> macro-XRT, macro-focal XRT;<sup>4</sup>  $\mu$ -XRT, micro-focal XRT;<sup>21</sup> nano-XRT, nano-focal XRT;<sup>22</sup> S-XRT, synchrotron-based XRT;<sup>23</sup> S-XRT-FL, S-XRT using Fresnel lens;<sup>24</sup> I-WFA-ICS, laser wake field accelerator-inverse Compton scattering;<sup>25</sup> scanning coherence diffraction microscopy or ptychography;<sup>26</sup> EC, Eddy current; CB-ECT, coil-based ECT;<sup>27</sup> SSS-ECT, solid state sensors-based ECT;<sup>29</sup> ECM, EC microscopy (focused EC,<sup>28</sup> SQUID<sup>33</sup> EC, etc.); EC-AFM, EC-atomic force microscopy;<sup>31</sup> OM, optical microscope; SEM, scanning electron microscope.

resolve indications in the depth direction, i.e., in the direction of wave propagation. The depth resolution is given by the pulse width of the ultrasonic signal. The pulse width is governed by the wavelength and the bandwidth of the ultrasonic pulse. Large bandwidth (damped transducer) and lower wavelength (higher frequency) pulses provide the best depth resolution, however, at the cost of penetrating power.

### A. Factors limiting resolution in UT

It can be seen in Fig. 1 that the ultrasound-based techniques (shown in different shades of green) cover the widest range of thickness as well as resolution achieved. It can also be seen that the resolution increases (worsens) with increasing depth at which the defect is located. In the case of conventional mono-element-based unfocused ultrasonic technique (UFUT), the increase in resolution with depth is primarily due to the increasing width of the ultrasonic beam with increasing propagation distance due to divergence. The divergence angle ( $\alpha/2$ ) of a transducer for a reduction in the

beam intensity to 50% (−6 dB) is given as<sup>1</sup>

$$\frac{\alpha}{2} = \sin^{-1} \left( \frac{0.51 \times \lambda}{D} \right) = \sin^{-1} \left( \frac{0.51 \times v}{f \times D} \right), \quad (1)$$

where  $\lambda$  is the wavelength of the ultrasonic wave,  $D$  is the diameter of the piezoelectric element,  $v$  is the velocity of the ultrasonic wave, and  $f$  is the frequency of the ultrasonic wave or the transducer. For a 2 MHz ultrasonic transducer of 10 mm element size, the calculated beam divergence angle ( $\alpha/2$ ) for 6 dB amplitude reduction is  $\sim 2.2^\circ$  in water and  $\sim 8.8^\circ$  in steel. The beam profile of a similar ultrasonic transducer obtained experimentally in the through-transmission mode using the probe as an emitter and a small, 1 mm diameter pinducer (CTS VP-1063 from CTS Corporation) as a receiver is shown in Fig. 2.<sup>35</sup> A divergence angle similar to that obtained theoretically is observed experimentally [Fig. 2(d)] beyond about 30 mm, which is the near field (NF) of the transducer given by

$$NF = \frac{D^2}{4\lambda}. \quad (2)$$

A continuous decrease in amplitude and an increase in beam width can be clearly visualized in Fig. 2, beyond the NF, i.e., in the far field region. The increasing beam width [Figs. 2(b) and 2(d)] leads to increased (poor) resolution in the far-field region.

In a steel component, the divergence is expected to be about 4 times ( $4 \times \alpha/2 = 8.8^\circ$ ) due to four times higher velocity and, hence, larger wavelength for the same frequency.

In addition to the increasing beam width with increasing depth leading to a deterioration of the resolution, the amplitude of an ultrasonic wave also decreases exponentially with increasing propagation distance.<sup>5</sup> The total attenuation coefficient ( $\alpha_T$ ) of the ultrasonic wave may be expressed as the sum of geometrical attenuation ( $\alpha_G$ ) due to beam spreading, interface losses, etc., and material attenuation ( $\alpha_M$ ) due to absorption ( $\alpha_A$ ) and scattering ( $\alpha_S$ ),

$$\alpha_T = \alpha_G + \alpha_M, \quad (3)$$

$$\alpha_M = \alpha_A + \alpha_S. \quad (4)$$

The absorption coefficient  $\alpha_A$  can be expressed as

$$\alpha_A = a_1 f^{0.5} + a_2 f + a_3 f^2, \quad (5)$$

where  $a_1$ ,  $a_2$ , and  $a_3$  are the constants and  $f$  is the frequency. The first, second, and third terms on the right-hand side of the equation take into account the thermoelastic losses, magnetic hysteresis losses, and losses due to dislocation damping, respectively. In a polycrystalline material, the material attenuation is primarily governed by grain scattering.<sup>5</sup> The ultrasonic scattering coefficient due to Rayleigh scattering (when  $\lambda \gg d$ ) in polycrystalline materials can be expressed as<sup>36</sup>

$$\alpha_s = S d^3 f^4, \quad (6)$$

where  $S$  is the scattering factor that depends on the elastic

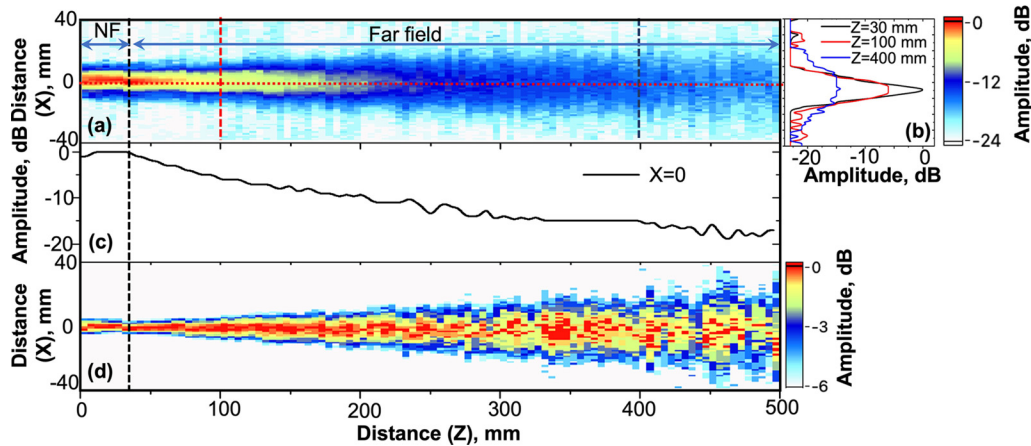


**FIG. 2.** (a) Beam profile map of a 2 MHz ultrasonic transducer of 10 mm diameter in water, measured using a 1 mm diameter pinducer; (b) the cross-sectional amplitude profiles at the near field (NF = 30 mm) distance and at distances of 100 and 400 mm from the probe face corresponding to vertical dotted lines marked in (a); (c) shows the longitudinal section beam profile along the probe center (at  $X=0$ ). A continuous decrease in amplitude beyond the near field can be seen in (b) and (c) due to beam divergence. Beam divergence can also be visualized in (d) showing the map of the amplitude normalized at all  $Z$  distances with the corresponding amplitude at  $X=0$ .

anisotropy and the longitudinal and transverse sound velocities,  $d$  is the average grain size in the material, and  $f$  is the frequency. It can be seen from Eqs. (5) and (6) that the attenuation increases with increasing frequency. Hence, for deeper penetration required in a thick material, lower frequency is required to be used. Furthermore, larger grain size leads to increased attenuation in cast structures. Similarly, large scattering factors combined with large grain size in austenitic stainless steels and nickel base alloys limit the highest frequency to be used to about less than 2 MHz only. This further leads to reduction in resolution with increasing object thickness.

## B. Improving resolution by beam focusing

### 1. Focusing using a lens

The first approach to improve the resolution is to decrease the beam width of the ultrasonic wave or divergence through focusing at the highest frequency limited by the penetration in the thickness of the object being inspected. Focusing not only helps in achieving improved lateral resolution but also leads to higher sensitivity and improved SNR. Many hardware- and software-based approaches aimed at focusing the sound beam have been developed over the years and have been successfully used for various industrial applications. Focusing using a suitable lens or a curved transducer has been very widely used in practical applications for inspection of components submerged in water, with the focal depth governed by lens geometry and ultrasonic velocity in the medium. By suitably changing the lens curvature, a beam can be focused at a point within the near field as given by Eq. (2). The  $-3$  dB focal spot beam size of a focused transducer is given by<sup>37</sup>

$$\delta_{-3dB} = \frac{\lambda F}{A} = \frac{v}{f} f^*, \quad (7)$$

where  $v$  is the velocity of sound in the medium,  $f$  is the frequency,  $F$  is the focal depth (defect depth),  $A$  is the maximum aperture equal to the diameter of the piezoelectric element in the case of a conventional mono-element ultrasonic transducer, and  $f^*(=F/A)$  is the  $f$ -number defining the focusing ability of the lens at a given frequency in a medium. It can be seen that the lateral resolution increases (i.e., worsens) with increasing depth and wavelength (decreasing frequency) and decreases (i.e., improves) with increasing transducer element size. However, owing to practical limitations, the diameter of the element is limited at higher frequency due to its reduced thickness with increasing frequency (element thickness  $= \lambda_p/2$ , where  $\lambda_p$  is the wavelength in the probe element). This limits the resolution achieved at larger depths. However, at shallow depths, high-frequency transducers can provide very high resolution. Frequencies in the range of 5–25 MHz have been used for inspection of mid-thickness (up to about 100 mm diameter) forge components with high resolution.<sup>38</sup> For non-ferrous die-cast metallic components, the limits of detection for pores have been worked and compared to measurements.<sup>39</sup>

The quest of obtaining images with acoustic contrast and equivalent resolution as that of an optical microscope ( $\sim 0.3 \mu\text{m}$ ) led to the development of a scanning acoustic microscope (SAM).<sup>13,14</sup> Early acoustic microscope comprised of a pair of focused immersion ultrasonic probes (a transmitter and a receiver) working in the through-transmission mode at the central frequency of 160 MHz with an acoustically transparent specimen placed at the focal point of the probes. At 160 MHz, a wavelength of about  $10 \mu\text{m}$  in water and a comparable resolution could be achieved. With the development of electronics, scanning devices, and high-frequency, high-power ultrasonic probes with the required lenses, SAM up to 1–2 GHz in the pulse-echo mode could be realized.<sup>40</sup> At these frequencies, the resolution achievable is  $\sim 1 \mu\text{m}$  on the surface of the specimen due to the shorter wavelength in water. This is schematically represented by a step in Fig. 1 for the



resolution observed in SAM at the surface as compared to just beneath the surface. In the acoustic microscope, the reflection amplitude,  $V(z)$ , as a function of probe distance from the specimen surface ( $z$ ) was used for the measurement of Rayleigh wave velocity and to explain the acoustic contrast.<sup>14</sup> Provided that the opening angle of the acoustic lens is large enough to include the critical angle for Rayleigh wave generation, the  $V(z)$  curve shows an oscillatory pattern due to the interference of the Rayleigh wave and the directly reflected longitudinal wave from the specimen surface. The contrast in the acoustic image caused by focusing the ultrasonic beam onto the specimen surface is due to the difference in the acoustic impedance (=density  $\times$  ultrasonic velocity).<sup>41</sup> However, a better contrast in the acoustic image is observed in the overfocused condition (probe-specimen distance is less than the focal distance) due to the contrast produced by the Rayleigh waves generated in the surface of the specimen.

Gilmore *et al.*<sup>42</sup> discussed the design of a SAM focusing lens immersed in water so that maximal penetration and maximal contrast are obtained from a flaw in a solid. The flaw size to be detected is the key design parameter for the lens that establishes the sensitivity for the non-destructive evaluation of a material volume. This flaw must block a sufficient fraction of the focused beam such that the signal back-reflected to the transducer is above a pre-defined signal-to-noise ratio (SNR), typically 3 dB. Taking into account diffraction of the ultrasonic beam at the surface of the material when entering the volume of the material, Gilmore *et al.*<sup>41</sup> derived

$$D_f \approx 2.4 \frac{\lambda_3 Z_f}{D'_L}, \quad (8)$$

where  $D_f$  is the ultrasonic beam diameter (null-to-null) at the defect,  $Z_f$  is its depth,  $\lambda_3$  is the wavelength in the specimen, and  $D'_L$  is the beam diameter at the surface of the specimen to be inspected, as shown in Fig. 3. Equation (8) holds for  $Z_f > D'_L$ . The SAM has been extensively used for studying biological samples and in electronic industries for detection of surface/subsurface defects.<sup>43</sup> Recent SAMs also called C-SAMs work more like conventional pulse-echo water immersion technique in the 50–200 MHz range providing surface resolution of 5–20  $\mu\text{m}$ .<sup>44</sup>

Unlike the curved conventional lenses described above, focusing can also be achieved with flat Fresnel zone plate (FZP) lenses as in the case of electromagnetic waves.<sup>45</sup> An FZP lens comprises of a set of concentric rings with decreasing distance acting as Fresnel regions and a  $\pi$  phase difference between consecutive regions. Dolmatov *et al.*<sup>46</sup> recently demonstrated applications of phase reversal (PR) FZP for high-resolution ultrasonic NDT.

## 2. Focusing without using a lens

The major limitations of conventional lens-based focusing of the ultrasonic beam are as follows: (i) they can be used only in the immersion setup (multi-layer flat face lens developed for focusing in contact were not very popular), (ii) the beam can be focused only within the near field defined by Eq. (2) and limited by the probe diameter, and (iii) focusing at different depths require different lenses. These limitations were overcome by employing the

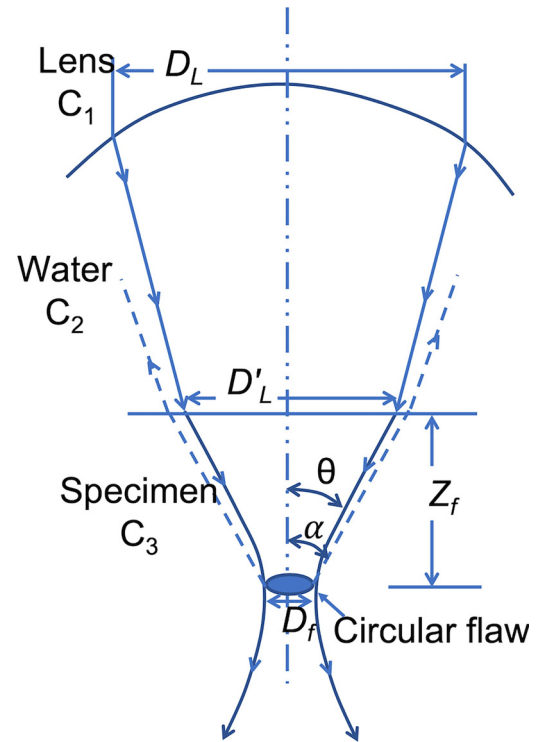


**FIG. 3.** Geometry of beam blocking flaw for the volumetric scan. Here,  $\theta$  and  $\gamma$  are the half angles of the converging incident beam and the back-reflected beam, respectively. Reprinted with permission from Philos. Trans. R. Soc. London Ser. A 320, 215–235 (1986). Copyright 1986 Royal Society Publishing.

synthetic aperture focusing technique (SAFT), which was adopted in UT from radar imaging applications.<sup>47,48</sup> The A-scans (time vs amplitude signals) at regular interval are acquired by scanning the component surface by a small diverging beam ultrasonic transducer. Knowing the ultrasonic velocity in the material and probe locations of data acquisition, suitable time delay and summation methodology are applied at every pixel location in the region of interest (ROI) to obtain a focused B-scan (cross-sectional view) image. The effective aperture size is equivalent to the scan distance, and hence, it is much larger as compared to that for a conventional focused ultrasonic transducer for which the aperture is the diameter of the piezoelectric element. This leads to focusing up to a much larger depth with improved resolution, as per Eq. (7). Furthermore, averaging of multiple A-scan signals also leads to improvement in the SNR. In addition to the total effective aperture and wavelength, the resolution achieved through the application of SAFT technique is also influenced by the size of the ultrasonic transducer. The best resolution achieved using SAFT is limited by  $D/2$ , where  $D$  is the diameter of the transducer.<sup>11</sup>

The use of a single small diameter transducer for obtaining a large diverging beam limits the penetration depth in SAFT. Furthermore, focusing is synthetically performed only in the reception side in SAFT. Phased array ultrasonic techniques (PAUT)

provided the means of focusing in the contact mode during both transmission and reception sequences. The advantages of PAUT over the traditional single element transducer are their ability to perform multiple inspections without the need for reconfiguration and also the potential for improved sensitivity and coverage. A linear PAUT transducer comprises of multiple tiny elements placed normally at a pitch of the order of  $\lambda/2$  to avoid side lobes. Using a multi-channel PA equipment, the transmission of these elements is individually controlled using suitable delay laws leading to a focused beam at the required depth due to constructive interference of beams emanated from individual elements. An inverse delay law is applied during reception. The focal spot size ( $W$ ) in PAUT for rectangular elements is given by Eq. (9) (Ref. 18) and is limited by the diffraction limit ( $\lambda/2$ ),

$$W = 0.61 \frac{\lambda}{\sin(\theta)} \approx 1.2 \frac{F\lambda}{A}, \quad (9)$$

where  $2\theta$  is the angle subtended by the aperture  $A$  at the focal spot at distance  $F$ , as shown in Fig. 4.

Due to a large aperture ( $A = np$ ,  $n$  is the number of elements and  $p$  is the pitch), high resolution governed by Eq. (9) nearing the Rayleigh limit can be achieved up to a much larger depth limited by the near field shown in Eq. (2).<sup>6</sup> Several variants of PAUT have been proposed.<sup>49–52</sup> Different variants of PAUT have specific advantages and limitations, such as conventional delay law-based focusing that provides best sensitivity but requires multiple firings to achieve focusing at all points in the region of interest (ROI), while the full-matrix capture (sequential single element transmission and reception by all elements) allows simultaneous focusing at all points in the ROI by post-processing but with reduced sensitivity. Focusing achieved at the same depth using similar aperture size and frequency exhibits comparable resolution by different beam forming approaches such as the focused sector scan, the full-matrix capture-total focusing method (FMC-TFM), and plane wave imaging (PWI) methods.<sup>50</sup> However, FMC-based technique

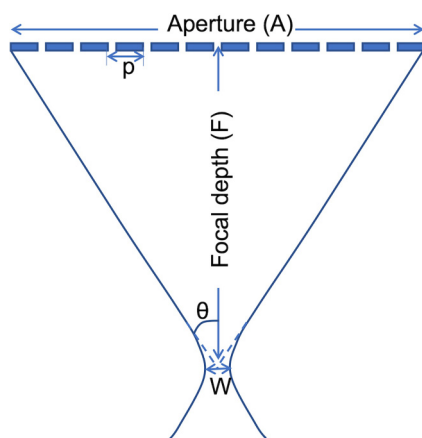


FIG. 4. Schematic of focal spot size in the phased array ultrasonic technique.

provides flexibility and opportunity to perform multi-modal imaging and post-processing with various different approaches due to a large volume of input data available.<sup>53</sup> The approach to achieve the best resolution in a phased array technique is to use a high-frequency transducer of a large aperture.

For enhancing the sensitivity achieved in an anisotropic medium, time-reversal mirror (TRM) based PAUT has also been proposed.<sup>51</sup> A time-reversed wave back propagates and refocuses at its initial source. However, it has been shown that the superimposition of the converging time-reversed wave and the reflecting diverging waves from the focal spot limits the focal spot size to  $\lambda/2$ , even for a point source smaller than  $\lambda/2$ .<sup>54</sup>

### C. Resolution beyond the diffraction limit

Various means of achieving resolution beyond the diffraction limit have been proposed. By utilizing second harmonics at nonlinear power levels, improvement in resolution by a factor of 1.4 has been demonstrated in the conventional SAM setup.<sup>55</sup>

Most of the other approaches in achieving subwavelength super-resolution in UT are near-field imaging techniques based on utilizing the evanescent waves of high frequency generated by interaction of the low-frequency incident wave with small defects ( $<\lambda/2$ ). The evanescent approach shows that a subwavelength resolution achieved is not in contradiction with the diffraction limit. However, these evanescent waves are non-propagative and decrease exponentially over roughly one wavelength. Hence, evanescent wave-based approaches work only for defects near the surface.

The evanescent wave was utilized in the TRM for achieving subwavelength resolution by replacing the source by its time-reversal image.<sup>56</sup> This new device acted as an acoustic sink that absorbed the time-reversed wave. With this approach of an acoustic sink, a focal spot size of less than 1/14th of one wavelength was recorded experimentally at an operating frequency of 500 kHz in a 1.9 mm thick transparent glass plate.

Amplification of the evanescent wave to achieve subwavelength resolution has been reported by several authors by using metamaterials.<sup>15–17</sup> Ambati *et al.*<sup>15</sup> proposed that the evanescent pressure fields scattered from an object could be resonantly coupled and enhanced at the surface of an acoustic metamaterial, resulting in an image with resolution below the diffraction limit. They demonstrated a resolution of  $\lambda/5$ . Sukhovich *et al.*<sup>16</sup> demonstrated experimentally and theoretically that super resolution could be achieved by imaging with a flat lens comprising of a phononic crystal exhibiting negative refraction. This phenomenon was related to the coupling between the incident evanescent waves and a bound slab mode of the phononic crystal lens, leading to amplification of evanescent waves by the slab mode. As expected, the super resolution was only observed when the source was located very near to the lens.

Recently, Amireddy *et al.*<sup>17</sup> experimentally demonstrated subwavelength ultrasonic imaging of defects in metallic samples using holey-structured metamaterial lenses. At 244 kHz incident ultrasonic wave ( $\lambda \approx 26$  mm for the longitudinal wave in the aluminum block), two side drilled holes (SDHs) of 1.5 mm diameter separated by 1 mm ( $\lambda/25$ ) at the depth of 2 mm from the detection surface could be clearly resolved. Optimal dimensions of the metamaterial's

geometric parameters were determined using numerical simulation and the physics of wave propagation through holey lenses. Amireddy *et al.*<sup>17</sup> also showed the extraordinary transmission capacity of holey-structured metamaterials by the coupling of higher frequencies in the incident ultrasonic wave field to resonant modes of the lens. The key to the success is the optimization of the geometric parameters of metamaterials to provide a suitable high-frequency resonant filter to allow evanescent waves to be detected with a high signal to noise ratio.

Application of a 3D printed metamaterial has been demonstrated for subwavelength imaging at the kHz frequency range.<sup>57</sup> Laureti *et al.*<sup>58</sup> utilized “trapped air” metamaterial, fabricated via vat photopolymerization for ultrasonic sub-wavelength imaging in water using polymeric metamaterials at 200–300 kHz. Even though the above two studies were performed in 10–100 s of the kHz frequency regime only, they show the potential of advance manufacturing technologies such as 3D printing/additive manufacturing in fabricating desired metamaterials for high-frequency range.

As discussed earlier, the subwavelength resolution achieved using evanescent waves is applicable only when the probing sensor is within the proximity ( $<\lambda$ ) of the defect, i.e., in the near-field zone. Chen and Chew<sup>59</sup> reported sub-wavelength resolution in the far-field zone in microwave experiments taking into account multiple scattering in the imaging algorithm. Similar approaches have also been adopted in ultrasonic imaging. Simonetti<sup>60</sup> described that the key to unravel the subwavelength world from the far-field pattern of a scattered wave is through tapping the information in multiple scattering. Simonetti<sup>18</sup> also demonstrated experimentally a subwavelength resolution of more than 2.5 times smaller than that predicted by the Rayleigh criterion for SDHs in the far-field (at 46 mm depth) in a carbon steel specimen using time reversal and the multiple signal classification (TR-MUSIC) method utilizing multiple scattering. The resolution better than the Rayleigh criterion by utilizing multiple scattering is described in terms of mode conversion of longitudinal waves to transverse waves, then multiple scattering of transverse waves and finally again mode-converted to longitudinal waves detected by an array transducer, which encodes the contribution from transverse waves. Fan *et al.*<sup>61</sup> showed that for the weak noise situation ( $\text{SNR} > 20$  dB), TR-MUSIC provides significantly enhanced lateral resolution when compared to the total focusing method (TFM), breaking the diffraction limit. However, for higher noise levels, the total focusing method is shown to be robust, while the performance of time-reversal MUSIC is degraded.

Recently, Song and Yang<sup>62</sup> proposed a deep learning-enhanced super-resolution ultrasonic beamforming approach that computationally exceeded the diffraction limit and led to visualization of subwavelength defects. The methodology comprised of first generating focused images using the TFM algorithm from the phased array FMC data and subsequently adopting a fully convolutional network (FCN) architecture to achieve super-resolution. They demonstrated that the deep learning super-resolution ultrasonic beamforming approach not only enabled visualization of fine structural features of subwavelength defects, but also outperformed the resolution achieved by the TR-MUSIC.

The best resolution in ultrasonic imaging, thus far, in the near-field region has been achieved by utilizing atomic force microscopy (AFM) combined with the possibility to detect

ultrasonic waves either in the contact-resonance of the cantilever or out of resonance. An AFM probe can have the tip radius of about 10 nm and, hence, provide the lateral resolution of this order for this type of the near-field acoustic microscope. A review of various ultrasonic-based AFM techniques for sub-surface acoustic imaging at nm scale can be found in Refs. 19 and 20. In addition to measuring elastic properties with a lateral resolution of less than 50 nm,<sup>63,64</sup> the AFM-based ultrasonic techniques have been used to detect sub-surface features (embedded inclusions, voids, etc.) and defects in highly oriented pyrolytic graphite (HOPG) samples, internal voids in integrated circuits, adhesive interfaces, and subcellular structures [see references in Ref. 19]. The contrast in the acoustic AFM is essentially generated due to effective change in contact stiffness due to the presence of defects in the sensing volume of the AFM tip. The change in contact stiffness is measured by the contact-resonance frequency relative to the free resonance of the cantilever. Furthermore, a GHz AFM technique to image sub-surface structures was proposed by Hu *et al.*<sup>65</sup> Micrometer-sized defects were insonified with 1 GHz ultrasonic waves (wavelength some  $\mu\text{m}$ ), which were amplitude modulated at a fraction or at a multiple frequency of a cantilever contact-resonance. The transmitted signals were demodulated by the nonlinear tip-surface interaction. Defects in the devices were imaged based on the contrast due to ultrasonic scattering and transmission differences determined by the acoustic mismatch between the host material and the defects, by their geometry, and by diffraction effects when traversing the buried structures.

It can be observed from the above discussion that the resolution ( $R$ ) in UT is primarily governed by the wavelength in a given technique. However, the ratio ( $R/\lambda$ ) ranges from  $\gg 0.5$  for conventional UT ( $R$  governed by the beam divergence),  $\sim 0.5$  in SAM and PAUT with smaller  $f$ -number [Eq. (7)],  $\sim 5$  for Time-Reversal-MUSIC,  $\sim 25$  for metamaterials-based UT, and about 10 000 in AFAM ( $R$  limited by contact radius). Even though a resolution of  $\lambda/25$  is reported in metamaterials-based UT, the absolute value of  $R$  of about 1 mm is only achieved due to low frequency employed, which is limited by the geometry of the metamaterial.

### III. X-RAY RADIOGRAPHIC TESTING (XRT)

The resolution ( $\approx \lambda/2$ ) in ultrasonic techniques limited by the Rayleigh criteria of diffraction arises from the wave nature of the ultrasonic energy. On the other hand, attenuation-based x-ray radiography (the most commonly used in NDT) probes a medium by exploiting the particle nature of electromagnetic radiation and the wave nature is only reflected at atomic scales (the Compton effect and Bragg scattering). In XRT, the wave nature of x rays is exploited in phase contrast imaging, which is particularly effective for low atomic weight elements such as for weakly attenuating soft tissue structures where attenuation-based conventional XRT provides low contrast.<sup>66</sup> In radiography techniques, the resolution is limited by various experimental conditions, most importantly to half the x-ray source (target) size (a few 10 s of nm to a few mm), which is normally orders of magnitude larger than the diffraction-limited resolution given by  $\lambda/2$  (0.005–5 nm).

With the advances in precise scanning mechanisms, computational facility and fast response detectors, viz., flat-panel and CCDs for high-energy x rays, computed tomography (CT) is becoming more popular for NDT applications also, in addition to the medical field. Kastner and Heinzl<sup>67</sup> discussed different size scales of heterogeneities and of the affected material volume requiring appropriate CT methods, scanning geometries, and resolutions. In order to quantify features of interest from CT scans, a major challenge is the analysis and visualization of the generated CT data. Advanced 3D-image processing techniques are needed for extraction and characterization of each single feature of interest. Different x-ray CT techniques having different spatial resolutions for imaging of objects of different thicknesses were reported. As the resolution achieved in XCT are similar to those observed in a single projection of XRT, the resolution values reported by Kastner and Heinzl<sup>66</sup> for XCT are also used in Fig. 1 for XRT. It can be seen that a very fine resolution may be obtained in thin specimens at low x-ray energy; however, resolution deteriorates for techniques amenable for larger object thicknesses.

Spatial resolution in XRT is normally expressed in line pairs that can be distinguished per mm (lp/mm). A line pair consists of a dark and a bright line produced in the x-ray image of an alternating layer of high- and low-density materials. The spatial resolution is measured in two different ways: (i) visual resolution tests using line group test patterns providing defined spatial frequencies and (ii) the quantitative measurement of the modulation transfer function (MTF), which relates the spatial frequency of sample features to the corresponding loss of contrast in their x-ray image. The  $MTF_{1/2}$  corresponding to a contrast loss of 50% is usually considered as a quantitative measure of resolution.<sup>21</sup>

### A. Factors affecting resolution in XRT

Radiography is a through transmission technique, i.e., the source and the detector are placed on opposite sides of the test object. Hence, the x-ray beam of sufficient energy and intensity is required to allow the through thickness penetration and imaging by the detector. Image quality in XRT is the total result of resolution/sharpness, contrast resolution and noise. Two important aspects in x-ray imaging are contrast and spatial resolution. They depend on many parameters like the size of the x-ray source, the size and the number of pixels in the detector, and the amount of shot noise and electronic noise of the detection system. For a micro-CT, a relation could be established linking the spatial sampling  $w$  with the contrast resolution  $\Delta\mu/\mu$ ,<sup>68</sup>

$$\frac{\Delta\mu}{\mu} w^2 = \text{const}, \quad (10)$$

where  $w = D/N$ , with  $D$  being the object diameter and  $N$  being the number of pixels. This relation was verified experimentally with different materials. The “const” reflects the details of the tomographic system. Experience shows that a density difference of 1% can be detected. This limit still belongs to the state of the art for standard and for micro-computed tomography systems. Both kinds of resolution are usually intertwined and the selection of an x-ray imaging system, such as radioscopy, computed tomography (CT),

x-ray microscopy, tomosynthesis, or digital laminography, for non-destructive testing of integrated circuit and ceramic parts are usually based on these two parameters. Industrial systems allow one to reach a resolution from  $50\mu\text{m}$  down to  $1\mu\text{m}$  and below based on new types of x-ray sources,<sup>69</sup> for example, carbon nanotube emitters. Materials can be analyzed in the range from plastics, ceramics to metals, with object diameters up to 300 mm. Further aspects of resolution, contrast, and scanning geometry of microtomography and its application in material science are discussed by Stock<sup>70</sup> and Vasarhelyi *et al.*<sup>71</sup>

Three factors govern the spatial resolution in XRT: (i) source size or focal spot size, (ii) magnification obtained, i.e., image size divided by the object size, and (iii) granularity of the film or pixel size of the detector. For example, in an x-ray image obtained at  $5\times$  magnification on a detector with  $50\mu\text{m}$  pixel size, a resolution of  $10\mu\text{m}$  can be obtained for a point x-ray source. However, with increasing the source/focal spot size, the resolution deteriorates due to increasing unsharpness. The geometrical unsharpness or blurring ( $B$ ) for a focal spot size of  $W$  at a magnification  $M = F_2/F_1$  (Fig. 5) is given as<sup>72</sup>

$$B = W(M - 1). \quad (11)$$

The effect of focal spot size on resolution achieved is shown schematically in Fig. 5. Two-point objects at the same separation are resolved clearly in the left image with smaller focal spot size, whereas the same is barely resolved in the right image with larger spot size.

Resolution ( $R$ ) in a radiography setup is given by the combined influence of the blurring ( $B$ ) and the pixel size of the detector ( $d$ ),

$$R = \frac{d+B}{M} = \frac{d}{M} + \frac{B}{M} = \frac{d}{M} + \left(1 - \frac{1}{M}\right)W. \quad (12)$$

It can be seen in Eq. (12) that the resolution at lower magnification is governed by  $d$ , whereas it is governed by  $W$  at higher magnifications. The resolution improves with decreasing  $d$ ; however, no improvement in resolution is obtained for pixel size smaller than  $W$ .<sup>71</sup> Thus, for a given pixel size of the detector, better resolution is obtained at higher magnification with smaller focal spots either through reducing the source size or through focusing. Increase in x-ray attenuation with increasing object thickness may be compensated to some extent by increasing tube power (voltage or current). However, increasing tube power deteriorates resolution by increasing the effective focal spot size,<sup>21</sup> leading to a trend of deteriorating resolution with increasing object thickness as shown in Fig. 1.

### B. Enhancing spatial resolution by reduction in source size

To meet the requirement of higher magnifications with finer resolution, x-ray systems with ever decreasing focal spot sizes have been developed over the years. But as the electron stream is focused to a smaller spot size, the power of the tube must be reduced to prevent overheating at the tube anode. Therefore, the focal spot size becomes a tradeoff of resolving capability and



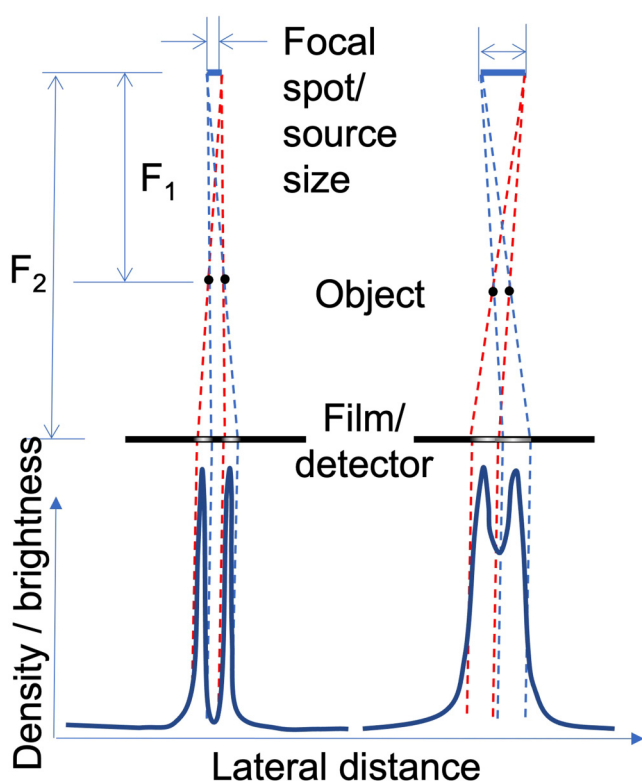


**FIG. 5.** Effect of focal spot size on the resolution achieved. Two-point objects at the same separation are resolved clearly in the left image with smaller focal spot size as compared to the right image.

power. X-ray generators can be classified as a conventional macro-focus ( $W \approx 0.5$  mm), minifocus ( $W \approx 0.05$ – $0.5$  mm), microfocus ( $W < 50$   $\mu\text{m}$ ), and nanofocus (a few 100 nm) systems. A standard micro-focus x-ray generator provides smaller focal spot size ( $< 2$   $\mu\text{m}$ ) in the through transmission mode as compared to that in the reflection mode. A considerably magnified x-ray image of a several hundred nanometer resolution has been achieved using the carbon nanotube (CNT) emitter.<sup>22</sup> The x-ray beam brightness is proportional to the electron-beam power density at the anode that is limited in the current rotating-anode and micro/nanofocus technology due to intrinsic thermal limitations. An anode concept, based on a liquid-metal jet (LMJ), with the potential to increase the brightness by 100 times due to inherently different thermal limitations was proposed by Hemberg *et al.*<sup>73</sup> The LMJs provide high brilliance in the energy upto  $\sim 50$  keV with  $\sim 50$   $\mu\text{m}$  focal spot size.

The spot size of x ray can be controlled as small as several micrometers in a lower energy range by x-ray generators. However, the high-energy (multi-MeV or much higher) x ray needed in the inspection of thick industry products can be obtained only by electron accelerator facility, in which the spot size of the electron beam is much bigger (usually several millimeters).<sup>74</sup> When the x ray is

generated by the Bremsstrahlung process, its spot size and also the spatial resolution are limited by the bigger spot size of the electron beam. The recent developments of the high-brightness MeV-photon source based on laser-wake-field accelerator-inverse Compton scattering (LWFA-ICS) has opened up exciting new possibilities for high-resolution radiography of dense thick objects.<sup>25</sup> The spatial resolution of much better than 2.5 lp/mm at energy in a couple of MeV range is demonstrated.

### C. Synchrotron-based x-ray imaging

A synchrotron source delivers x-ray beams with intensity more than three orders of magnitude higher than that of a tabletop x-ray source.<sup>75</sup> The high intensity or brightness of synchrotron x-ray beams leads to faster imaging, therefore dramatically improves the temporal resolution to the seconds-level for a microtomography beamline<sup>76</sup> and to the minutes level for a nanotomography beamline.<sup>77</sup>

At synchrotron sources, the x-ray beam is almost parallel, making geometrical magnification impossible without using a lens. However, the high flux can be detected by a thin scintillator screen, converting x rays to visible light. This allows the use of optical magnification lenses to achieve high resolution.<sup>78</sup> As the wavelength of the x rays is in the nm to sub-nm range, the diffraction limited spatial resolution of transmission x-ray microscopy (TXM) can be in the nm range, if a suitable x-ray lens could be used. However, difficulty in fabrication of suitable x-ray lenses has limited the progress of developing TXMs with nm scale resolution. With advanced nanofabrication technologies, e.g., high aspect ratio nanoscale lithography and controlled high precision layer deposition and polishing, significant progress has been made in fabricating x-ray lenses for TXM in recent years.<sup>24,79</sup>

In a typical TXM setup using a synchrotron source, a capillary condenser is used to provide a hollow-cone-beam illumination on the sample and an x-ray lens is inserted between the sample and the detector as an objective lens to achieve a desired magnification.<sup>80</sup> Out of the different types of x-ray lenses available such as Fresnel zone plates (diffractive), mirrors, and refractive lenses, the Fresnel zone plates exhibit the best resolution and modulation transfer function (MTF). Fresnel zone plates provide spatial resolutions of 15–20 nm in the soft and of about 30–50 nm in the hard x-ray energy range.<sup>24</sup> The reason for the lower resolution in the latter case is due to higher penetrating power of the hard x rays. Using interlaced zone plate optics, a resolution in the range of 10 nm was achieved recently.<sup>81</sup> In a conventional TXM, the spatial resolution is limited by aberrations and the limited numerical apertures of the x-ray optics. By combining scanning microscopy with coherent x-ray diffraction imaging, this limit has been overcome in scanning coherent diffraction microscopy, also known as ptychography.<sup>26</sup> Schropp *et al.*<sup>26</sup> have demonstrated a 10 nm spatial resolution, clearly exceeding the resolution limits of conventional hard x-ray microscopy, using a hard x-ray scanning microscope built at a synchrotron radiation source.

Another major advantage of a synchrotron x-ray source is its energy tunability over a wide range. By conducting tomography at selected energy levels near the absorption edges of the selected elements, compositional and chemical sensitivity can be achieved in

the technique called as x ray near absorption edge spectroscopy (XNAES) which enhances the contrast resolution significantly.<sup>80,82</sup>

#### D. Super-resolution imaging

Super-resolution imaging corresponds to achieving resolution better than that obtained by the detector using suitable post-processing of the projection x-ray images. This is particularly useful in the case of under-sampled images where resolvable structures are imaged to sub-pixel sizes. Super-resolution can be obtained either using a set of low-resolution images with different image contents or through applications of artificial neural networks (ANNs) on a single image.

Lübcke *et al.*<sup>83</sup> reconstructed super-resolution images (SRIs) from a set of  $4 \times 4$  individual low-resolution images that were recorded for different sub-pixel shifts of the detector. The algorithm comprises of applying a Tukey window to avoid boundary effects, followed by measuring and suitably correcting the rotational and lateral shifts in individual images to obtain an SRI. They reported SRIs with a 1.3 times higher resolution than that for the individual low-resolution images, which are close to the maximum achievable enhancement factor of about 1.5 in the x-ray regime under ideal conditions.<sup>83</sup>

Adopting from the recent developments in deep learning techniques in computer vision applications,<sup>84</sup> convolutional neural network (CNN)-based tools are being used recently for denoising and achieving super-resolution in x-ray projection<sup>85</sup> and CT images.<sup>86</sup> Enhancement in the lateral resolution by a factor of 2 is obtained by various CNNs.<sup>86</sup> Super-resolution imaging using CNN can help in substantial reduction in the data acquisition time for the same material volume coverage, while maintaining similar final resolution.

### IV. EDDY CURRENT TESTING (ECT)

Eddy current testing is a widely used NDT technique for inspection of electrically conductive materials for detection of surface/sub-surface defects.

#### A. Factor affecting resolution in ECT

In the most commonly used experimental setup of ECT, a coil carrying alternating current induces eddy current in the test specimen by coupling the time varying primary magnetic field generated by the coil. The eddy current in the specimen induces a secondary magnetic field that opposes the primary magnetic field. A change in the secondary field caused by perturbations in the eddy currents due to the presence of a defect on the surface or in the sub-surface region of the test material is used for defect detection. The secondary field is either measured by the change in the impedance of the same exciter coil or another receiver coil placed in its vicinity. The induced voltage,  $V_i$ , in a coil due to an alternating magnetic field is given by

$$V_i = -n \frac{d\phi}{dt}, \quad (13)$$

where  $n$  is the number of turns in the coil and  $\phi$  is the flux of the secondary magnetic field. It can be seen in Eq. (13) that the induced voltage and, thus, the sensitivity increase with the increasing number

of turns,  $n$ ; however, it also leads to an increase in the foot print leading to reduction in the lateral resolution. Furthermore, increasing rate of change of flux (increasing test frequency) increases the sensitivity but decreases the sensing depth and the depth of penetration as given by the following equation:

$$\delta = \frac{1}{\sqrt{\pi f \sigma \mu}}, \quad (14)$$

where  $\delta$  is the standard depth of penetration or skin depth at which the eddy current density decreases by the factor of  $e$  as compared to that at the surface,  $f$  is the test frequency,  $\sigma$  is the electrical conductivity in the specimen, and  $\mu = \mu_0 \times \mu_r$ , with  $\mu_0$  and  $\mu_r$  being the permeability of free space and relative permeability of the specimen, respectively. Owing to the skin effect, ECT is a surface/sub-surface technique. Equation (14) provides the depth of penetration for a plane wave incident on a conducting half space. Blodgett *et al.*<sup>28</sup> showed through experiment and theoretical studies that for an eddy current (EC) probe of finite dimension and at a lower operating frequency, Eq. (14) only provides the upper limit of the depth of penetration and the real depth of penetration is governed by the dimensions of the coil.

The resolution in an ECT technique is primarily governed by the lateral distribution of the eddy current decided by the transmitter (drive) coil and the foot print of the receiver (sensing) coil. Blodgett *et al.*<sup>28</sup> observed that the radial/lateral penetration depth or spread for a surface pancake type coil can be approximated as the sum of  $\delta$  and the effective coil diameter, which depends upon the size and to some extent on the shape of the coil. It is also possible to generate a highly focused field by using a single wire as a transmitter.<sup>30</sup> However, the depth of penetration is limited, and therefore, a sensitive pick-up sensor is required.

#### B. Improving resolution in coil-based ECT

The lateral distribution of EC generated by a small pancake type air core eddy current probe in a specimen is essentially governed by the probe diameter and to a modest extent only on the operating frequency.<sup>28</sup> Hence, the obvious choice for improving the resolution of a surface EC probe is to decrease the diameter of the probe/transmitting coil. Conversely, the size of the receiver coil should also be reduced to improve its foot print and, thus, the spatial resolution in the case of a probe with separate transmitter and receiver coils. Using an array of transmitter/receiver coils etched on a Kapton film, a resolution of  $350 \mu\text{m}$  is reported.<sup>31</sup>

The lateral resolution in ECT can be improved by confining the magnetic field as much as possible to a restricted area below the sensor. This can be performed by surrounding the probe with a highly conducting material to shield the eddy current and using a ferrite core to focus the magnetic field. Improvement in resolution by about 4 times is reported by Placko and Dufour<sup>87,88</sup> by focusing the magnetic field by using a ferrite core in place of the air core for a cup-type EC probe.<sup>87</sup> Using a pair of small solenoid EC coils of 70 turns of  $32 \mu\text{m}$  diameter copper wire on a mechanically sharpened core of a poly-crystalline iron needle of 0.3 mm working in differential mode, Yamazaki and Aono<sup>29</sup> obtained a conductivity map with the lateral resolution of 140 nm in diameter. In high-

resolution EC imaging, it is imperative to maintain the distance (lift-off) between the probe and the specimen. A piezo-scanner was used to maintain the separation of about 100 nm between the needle tip and the sample surface.<sup>31</sup>

### C. Solid state sensors as ECT receivers

Eddy currents in a specimen can only be induced inductively using a transmitting coil carrying an alternating current or an oscillating magnetic probe. However, the pick-up probe can be replaced by any other type of magnetic sensor of high resolution and sensitivity. Many types of solid-state magnetic sensors, such as Hall devices,<sup>89</sup> magneto-resistive (MR)<sup>90</sup> sensors (tunneling-/spin-polarized-, giant-, and anisotropic-MR), and magneto-impedance sensors,<sup>91</sup> have been used in ECT instead of pickup coils. As seen in Eq. (13), the induced voltage in an EC receiver probe is proportional to the rate of change in the flux. Hence, their sensitivity decreases with decreasing frequency, which leads to reduced sensitivity for deeper sub-surface defect that can be detected only at lower frequency [Eq. (14)]. Conversely, magneto-resistance-based solid state sensors such as Giant MR (GMR) or tunnel MR (TMR) sensors directly measure the magnetic field, independent of its frequency. This allows operation from dc to very high frequencies with very high sensitivity. Furthermore, unlike coil-based ECT receivers, the MR sensors detect the flux density and not the rate of flux change. Hence, the miniaturization of MR probe sensors is possible without losing their sensitivity. The small size and foot-print of MR sensors as receivers provide improved lateral resolution as compared to coil-based receiver sensors. The GMR/TMR sensors of 60  $\mu\text{m}$  size have been used in EC array sensors in combination with a single wire transmitter to achieve a resolution of about 0.3 mm for side drilled holes at about 0.25 mm depth in an aluminum sample.<sup>30</sup> A combination of a single wire transmitter and MR-based receivers has been reported by Tsukada *et al.*<sup>92</sup> and Wincheski *et al.*<sup>93</sup> Due to their very small foot-print, MR sensors are mostly used as an array for a large coverage and imaging of the specimen with minimal physical scanning. Using a current foil transmitter and a set of 22 GMRs array probes, a 2.2 mm width has been imaged at a spatial resolution of 70  $\mu\text{m}$ .<sup>31</sup>

In addition, superconducting quantum interference devices (SQUIDS) have also been used as the receiving sensor in eddy current application.<sup>33</sup> With a SQUID, one can measure very small magnetic fields as small as  $2 \times 10^{-15}$  T. Black and Wellstood<sup>94</sup> used a scanning magnetic flux microscope based on the high-temperature superconductor  $\text{YBa}_2\text{Cu}_3\text{O}_7$  SQUID to produce magnetic images of eddy currents in patterned Cu thin films and 11–30 pm thick Cu on printed circuit boards. The fields produced by the eddy currents were imaged with a spatial resolution of about 80  $\mu\text{m}$  over a 100 mm<sup>2</sup> sample area.

### D. AFM-based EC microscopy

If the sensor tip of an atomic force microscope cantilever is magnetic [as in the case of magnetic force microscopy (MFM)] and oscillates above a conducting material, it induces eddy currents. The resulting electrodynamic interaction between the sample and the sensor tip influences the cantilever vibrations so that local

variations in conductivity of a sample lead to phase shifts and/or amplitude changes that might be used to image the local conductivity. A lateral resolution of about 100 nm was reported by Hoffmann *et al.*<sup>95</sup> in the EC microscopy (ECM) performed using a magnetic AFM tip on an  $\text{Al}_2\text{O}_3$  sample containing TiC particles. In addition to ECM on a non-magnetic conducting material using a magnetic AFM tip, ECM has also been demonstrated on a ferromagnetic material using a non-magnetic conducting tip.<sup>95</sup> However, the contrast in the later is much smaller as compared to those obtained using a magnetically coated tip.

Due to a very thin coating of a ferromagnetic material on the MFM cantilever, the intensity of eddy current induced in the specimen due to an oscillating MFM cantilever is very low leading to low sensitivity to conductivity variations. Two possible ways of improving the sensitivity by enhancing the eddy current intensity are proposed: (i) by increasing the magnetic strength of the tip<sup>96</sup> and (ii) by inducing eddy current in the sample externally.<sup>32</sup> Lanz *et al.*<sup>96</sup> used the former method and improved the sensitivity drastically by gluing spherical FeNdBLa particles of radii ranging from 650 to 1000 nm onto the tips of commercial AFM cantilevers. The resolution was given by the extent of the stray-field of the magnetic tip, here about 0.7  $\mu\text{m}$ . The use of smaller particles results in a reduction in the magnitude of the stray field and, thus, to a reduction in the sensitivity to conductivity variations as well. The contrast in AFM-based ECM has been improved dramatically by exciting additionally eddy currents in the conductor by a small coil, independent of tip oscillations.<sup>32</sup> The tip of the cantilever was coated with a magnetic film and its nominal diameter was 20–30 nm. Again, an electrical conductivity image can be obtained by measuring the oscillations of the AFM cantilever at its eigenmodes, which were excited by tuning the frequency of the eddy current correspondingly. The contrast of the image is also determined by the interaction with the spatial distribution of the eddy currents when scattered at inhomogeneities. Although the strength of this interaction is independent of the tip's stray field, the resolution is now given by this field, i.e., by the distribution of evanescent waves,  $\sim 25$  nm.<sup>32</sup> Both techniques are near-field techniques.

Deriving from the design of the MFM, an Electro-Mechanical Eddy Current System (EMECS) probe was developed by Cherry *et al.*<sup>97</sup> to fill the resolution gap between an AFM-based ECT and a conventional coil-based ECT. The probe comprises of a sharpened magnetic tip attached to the membrane of an electret microphone. The magnet is actuated by an external coil with a low current AC voltage and the oscillating magnet acts as both source and detector for time varying magnetic field and in-turn eddy current in an electrically conducting sample.

Most of the ECM techniques discussed above have been experimentally demonstrated only for surface features. However, these techniques will still detect subsurface features due to electromagnetic nature but with reduced sensitivity and resolution as indicated in Fig. 1.

## V. SUMMARY AND PERSPECTIVE FOR HIGH RESOLUTION IN NDT

The factors limiting the resolution in three most popular NDT techniques, viz., UT, XRT, and ECT, are discussed following the

developments to achieve higher resolutions. An intertwining of sensitivity and resolution is observed in most of the techniques. A perspective for future trends in the three techniques is presented below.

Recent advances in PAUT in the last two decades have clearly demonstrated that PAUT outperforms conventional UT not just in terms of providing rapid imaging without physical scanning but also due to an improved resolution and SNR at larger depths at similar operating frequency. However, the PAUT is currently limited to below 20 MHz due to the smaller pitch size required at higher frequency. With decreasing width of the elements, the transmission energy also decreases. High-frequency phased array probes manufactured with advanced fabrication techniques, viz., 3D printing, sputtering, or deposition techniques, using high efficiency piezoelectric materials may be a possible solution to improve resolution at larger depths, at least for low attenuating materials including medical imaging.<sup>98</sup> Such a high-frequency system will also be very useful in acoustic microscopy. A few initial attempts have been made toward this recently<sup>98,99</sup> with different approaches, such as a 100 MHz polyurea film-based 32 element PAUT transducer was realized using higher harmonics<sup>98</sup> and a 56 MHz 128 element transducer using piezoelectric ceramic PZT 5H was fabricated using a gas flow sputtering process and associated-high frequency electronics were also developed.<sup>99</sup>

Almost all the metamaterials-based sub-wavelength imaging has been demonstrated at very low frequencies perhaps due to limitation in geometrical dimensions of the metamaterials. Sub-wavelength imaging at higher frequencies will really lead to gain in terms of absolute resolution. Again, advanced manufacturing techniques may provide solution in fabricating metamaterials supporting amplification of very short wavelength acoustic waves. Most of the near-field acoustic techniques require physical scanning of detectors, such as AFM-based techniques, SAM, and metamaterials-based subwavelength imaging require scanning of the AFM cantilever, acoustic lens, and laser or microphone-based detectors, respectively. One can visualize a high-frequency acoustic camera comprising a 3D printed/additively manufactured fine metamaterial giving a few  $\mu\text{m}$  resolution and a high-frequency matrix (2D) phased array ultrasonic transducer on top to electronically scan the metamaterial to obtain an image at high-resolution without physical scanning. Such a high-resolution microscopy system will be very useful in semiconductor industries where ever decreasing dimensions pose challenges to existing NDE techniques. For high-resolution ultrasonic inspection of critical thick components as required for thick rotors and their weld joints<sup>51</sup> of power plants, full matrix capture (single element or plane wave transmission) based PAUT techniques with large flexible aperture are going to thrive for future inspections.

The highest resolution in imaging of elastic, magnetic, and EC-based techniques can only be obtained in AFM-based near-field techniques. However, with its current limitations in field applications, array-based imaging can be the immediate solution of achieving the best possible resolution. In the field of eddy current NDT, array-based imaging using miniaturized focused transmitting/receiving sensors with printed/etched coils or using solid state receivers is expected to be the future for fast and high-resolution surface/sub-surface practical NDT applications for detection and

characterization of fine cracks in critical structures including small diameter steam generator tubes in nuclear power plants.<sup>100</sup>

The capability of graphical processing units (GPU) based multi-core parallel processing systems has already been tapped in the last decade for data processing and image reconstruction with high frame rates.<sup>101,102</sup> Such systems are also very effective in ANN applications and pave a path for real-time implementation of ANN in NDT fields for applications in image reconstruction, automatic analysis, as well as in achieving super-resolution with high frame rates.

## AUTHOR DECLARATIONS

### Conflict of Interest

The authors have no conflicts to disclose.

### Author Contributions

**Anish Kumar:** Conceptualization (lead); Data curation (lead); Formal analysis (lead); Visualization (lead); Writing – original draft (lead); Writing – review & editing (equal). **Walter Arnold:** Data curation (equal); Writing – review & editing (equal).

## DATA AVAILABILITY

The data that support the findings of this study are available from the corresponding author upon reasonable request.

## REFERENCES

- <sup>1</sup>J. Krautkrämer and H. Krautkrämer, *Ultrasonic Testing of Materials* (Springer-Verlag, Berlin, NY, 1990).
- <sup>2</sup>N. Bowler, *Eddy-Current Nondestructive Evaluation* (Springer, New York, 2019).
- <sup>3</sup>D. J. Hagmaier, *Fundamentals of Eddy Current Testing* (American Society for Nondestructive Testing, Columbus, OH, 1990).
- <sup>4</sup>R. Halmshaw, *Industrial Radiology* (Springer, Dordrecht, 1995).
- <sup>5</sup>A. Kumar, T. Jayakumar, and B. Raj, *Philos. Mag. A* **80**, 2469–2487 (2000).
- <sup>6</sup>Sumana and A. Kumar, in *Advances in Non-Destructive Evaluation. Lecture Notes in Mechanical Engineering*, edited by C. K. Mukhopadhyay and R. Mulaveesala (Springer, Singapore, 2021), pp. 329–339.
- <sup>7</sup>R. S. Gilmore, *J. Phys. D: Appl. Phys.* **29**, 1389–1417 (1996).
- <sup>8</sup>G. Canella, F. Monti, L. Pedicelli, and A. L'Erede, *NDT Int.* **16**, 151–153 (1983).
- <sup>9</sup>G. A. Gordon, S. Canumalla, and B. R. Tittmann, *Ultrasonics* **31**, 373–380 (1993).
- <sup>10</sup>S. F. Burch and J. T. Burton, *Ultrasonics* **22**, 275 (1984).
- <sup>11</sup>R. N. Thomson, *Ultrasonics* **22**, 9–15 (1984).
- <sup>12</sup>F. Dupont-Marillia, M. Jahazi, S. Lafreniere, and P. Belanger, *NDT E Int.* **103**, 119–129 (2019).
- <sup>13</sup>R. A. Lemons and C. F. Quate, *Appl. Phys. Lett.* **24**, 163–165 (1974).
- <sup>14</sup>A. Briggs and O. Kolosov, *Acoustic Microscopy* (Oxford University Press, Oxford, 2009).
- <sup>15</sup>M. Ambati, N. Fang, C. Sun, and X. Zhang, *Phys. Rev. B* **75**, 195447 (2007).
- <sup>16</sup>A. Sukhovich, B. Merheb, K. Muralidharan, J. O. Vasseur, Y. Pennec, P. A. Deymier, and J. H. Page, *Phys. Rev. Lett.* **102**, 154301 (2009).
- <sup>17</sup>K. K. Amireddy, K. Balasubramaniam, and P. Rajagopal, *Sci. Rep.* **7**, 7777 (2017).
- <sup>18</sup>F. Simonetti, *Appl. Phys. Lett.* **89**, 094105 (2006).
- <sup>19</sup>C. Ma and W. Arnold, *J. Appl. Phys.* **128**, 180901 (2020).
- <sup>20</sup>H. J. Sharahi, M. Janmaleki, L. Tetard, and G. J. Verbiest, *J. Appl. Phys.* **129**, 030901 (2021).



- <sup>21</sup>J. Rueckel, M. Stockmar, F. Pfeiffer, and J. Herzen, *Appl. Radiat. Isotop.* **94**, 230–234 (2014).
- <sup>22</sup>S. Park, J.-T. Kang, J.-W. Jeong, J.-W. Kim, K. N. Yun, H. Jeon, E. Go, J.-W. Lee, Y. Ahn, J.-H. Yeon, S. Kim, and Y.-H. Song, *IEEE Electron Device Lett.* **39**, 1936–1939 (2018).
- <sup>23</sup>H. Toda, F. Tomizato, F. Zeismann, Y. Motoyashiki-Besel, K. Uesugi, A. Takeuchi, Y. Suzuki, M. Kobayashi, and A. Brueckner-Foit, *ISIJ Int.* **52**, 516–521 (2012).
- <sup>24</sup>E. Zschech, W. Yun, and G. Schneider, *Appl. Phys. A* **92**, 423–429 (2008).
- <sup>25</sup>D. Haden, S. Chen, B. Zhao, P. Zhang, G. Golovin, W. Yan, C. Fruhling, S. Banerjee, and D. Umstadter, “Advances in laboratory-based x-ray sources, optics, and applications V,” in *Proceedings of SPIE Vol. 9964*, edited by A. M. Khounsary and G. E. van Dorssen (SPIE, 2016), p. 99640G.
- <sup>26</sup>A. Schropp, R. Hoppe, J. Patommel, D. Samberg, F. Seiboth, S. Stephan, G. Wellenreuther, G. Falkenberg, and C. G. Schroer, *Appl. Phys. Lett.* **100**, 253112 (2012).
- <sup>27</sup>C. V. Dodd and W. E. Deeds, *J. Appl. Phys.* **39**, 2829–2838 (1968).
- <sup>28</sup>M. Blodgett, W. Hassan, and P. B. Nagy, *Mater. Eval.* **58**, 647 (2000).
- <sup>29</sup>T. Yamazaki and M. Aono, *Mater. Trans.* **43**, 3217–3221 (2002).
- <sup>30</sup>M. Pelkner, R. Pohl, T. Erthner, R. Stegemann, M. Kreutzbruck, N. Sergeeva-Chollet, F. Cardoso, S. Freitas, P. Freitas, D. M. Caetano, J. Fernandes, M. Piedade, and J. Paul, in *Proceedings of 7th International Symposium on NDT in Aerospace*, Bremen, 16–18 November 2015 (German Society for Non-Destructive Testing, Berlin, Germany, 2015), pp. 1–8; available at <https://www.ndt.net/article/aero2015/papers/we5a4.pdf>
- <sup>31</sup>B. Marchand, F. Vacher, C. G. Pascaud, J. M. Decitre, and C. Fermon, *AIP Conf. Proc.* **975**, 313–320 (2008).
- <sup>32</sup>V. Nalladega, S. Sathish, K. V. Jata, and M. P. Blodgett, *Rev. Sci. Instrum.* **79**, 073705 (2008).
- <sup>33</sup>P. Seidel, S. Wunderlich, F. Schmidl, L. Dorrer, S. Linzen, F. Schmidt, F. Schrey, C. Steigmeier, K. Peiselt, S. Muller, A. Forster, S. Losche, and S. Gudochnikov, *IEEE Trans. Appl. Supercond.* **11**, 1176–1179 (2001).
- <sup>34</sup>S. G. Lipson and H. Lipson, *Optical Physics* (Cambridge University Press, Cambridge, 1981).
- <sup>35</sup>G. M. S. K. Chaitanya and A. Kumar, *Nucl. Eng. Des.* **325**, 184–191 (2017).
- <sup>36</sup>E. P. Papadakis, *J. Acoust. Soc. Am.* **37**, 711–717 (1965).
- <sup>37</sup>M. Vogt, J. Opretzka, C. Perrey, and H. Ermer, *Proc. Inst. Mech. Eng. Part H: J. Eng. Med.* **224**, 225–240 (2010).
- <sup>38</sup>D. C. Copley and P. J. Howard, in *Review of Progress in Quantitative NDE Vol. 14*, edited by D. O. Thompson and D. E. Chimenti (Plenum Press, New York, 1995), pp. 2145–2151.
- <sup>39</sup>S. Hirsekorn, U. Rabe, D. Bruche, N. Grov, T. Kinzle, and W. Arnold, *Casting Plant Technol. Int.* **4**, 28–33 (2007).
- <sup>40</sup>C. F. Quate, A. Atalar, and H. K. Wickramasinghe, *Proc. IEEE* **67**, 1092–1114 (1979).
- <sup>41</sup>S. Hirsekorn, S. Pangraz, G. Weides, and W. Arnold, *Appl. Phys. Lett.* **67**, 745–747 (1995).
- <sup>42</sup>R. S. Gilmore, K. C. Tam, J. D. Young, and D. R. Howard, *Philos. Trans. R. Soc. London Ser. A* **320**, 215–235 (1986).
- <sup>43</sup>W. Arnold, in *Reference Module in Materials Science and Materials Engineering*, edited by S. Hashmi (Elsevier, Oxford, 2019), pp. 1–4.
- <sup>44</sup>J. S. Brand, A. Lapadatu, T. Djuric, P. Czurratis, J. Schischka, and M. Petzold, *Micro/Nanolith. MEMS MOEMS* **13**, 011207 (2014).
- <sup>45</sup>D. Tarrazó-Serrano, S. Pérez-López, P. Candelas, A. Uris, and C. Rubio, *Sci. Rep.* **9**, 7067 (2019).
- <sup>46</sup>D. O. Dolmatov, D. Tarrazó-Serrano, G. A. Filippov, A. Uris, and D. A. Sednev, *Sensors* **21**, 7792 (2021).
- <sup>47</sup>G. S. Kino, M. Grant, P. D. Corl, and C. S. De Silets, in *IEEE 1979 Ultrasonics Symposium Proceedings* (IEEE, 1979), pp. 459–467.
- <sup>48</sup>V. Schmitz and W. Müller, in *Acoustical Imaging*, edited by W. Arnold and S. Hirsekorn (Springer, Dordrecht, 2004), pp. 57–68, 27.
- <sup>49</sup>Sumana and A. Kumar, *NDT E Int.* **116**, 102324 (2020).
- <sup>50</sup>P. Nanekar, A. Kumar, and T. Jayakumar, *Nondestruct. Testing Eval.* **30**, 105–123 (2015).
- <sup>51</sup>Sumana, S. Pongseerivasan, and A. Kumar, *Trans. Indian Inst. Met.* **74**, 499–510 (2021).
- <sup>52</sup>M. Fink, *IEEE Trans. Ultrason. Ferroelectr. Freq. Control* **39**, 555–566 (1992).
- <sup>53</sup>C. Holmes, B. W. Drinkwater, and P. D. Wilcox, *NDT&E Int.* **38**, 701–711 (2005).
- <sup>54</sup>D. Cassereau and M. Fink, *IEEE Trans. Ultrason. Ferroelectr. Freq. Control* **39**, 579–592 (1992).
- <sup>55</sup>D. Rugar, *J. Appl. Phys.* **56**, 1338–1346 (1984).
- <sup>56</sup>J. de Rosny and M. Fink, *Phys. Rev. Lett.* **89**, 124301 (2002).
- <sup>57</sup>S. Laureti, D. A. Hutchins, L. A. J. Davis, S. J. Leigh, and M. Ricci, *AIP Adv.* **6**, 121701 (2016).
- <sup>58</sup>S. Laureti, D. A. Hutchins, L. Astolfi, R. L. Watson, P. J. Thomas, P. Burrascano, L. Nie, S. Freear, M. Askari, A. T. Clare, and M. Ricci, *Sci. Rep.* **10**, 10601 (2020).
- <sup>59</sup>F.-C. Chen and W. C. Chew, *Appl. Phys. Lett.* **72**, 3080–3082 (1998).
- <sup>60</sup>F. Simonetti, *Phys. Rev. E* **73**, 036619 (2006).
- <sup>61</sup>C. Fan, M. Calep, M. Pan, and B. W. Drinkwater, *Ultrasonics* **54**, 1842–1850 (2014).
- <sup>62</sup>H. Song and Y. Yang, *NDT&E Int.* **116**, 102344 (2020).
- <sup>63</sup>A. Kumar, U. Rabe, S. Hirsekorn, and W. Arnold, *Appl. Phys. Lett.* **92**, 183106 (2008).
- <sup>64</sup>M. Kalyan Phani, A. Kumar, W. Arnold, and K. Samwer, *J. Alloys Compd.* **397**, 676 (2016).
- <sup>65</sup>S. Hu, C. Su, and W. Arnold, *J. Appl. Phys.* **109**, 084324 (2011).
- <sup>66</sup>L. C. P. Croton, K. S. Morgan, D. M. Paganin, L. T. Kerr, M. J. Wallace, K. J. Crossley, S. L. Miller, N. Yagi, K. Uesugi, S. B. Hooper, and M. J. Kitchen, *Sci. Rep.* **8**, 11412 (2018).
- <sup>67</sup>J. Kastner and C. Heinzl, in *Integrated Imaging and Vision Techniques for Industrial Inspection, Advances in Computer Vision and Pattern Recognition*, edited by L. Zheng, H. Ukida, P. Ramuhalli, and K. Niel (Springer, London, 2015), pp. 227–250.
- <sup>68</sup>T. Vontz, K. Goebbels, M. Maisl, H. Reiter, and S. Hirsekorn, in *Review of Progress in Quantitative Nondestructive Evaluation*, edited by D. O. Thompson and D. E. Chimenti (Plenum Press, 1988), pp. 389–397, 7A.
- <sup>69</sup>R. J. Parmee, C. M. Collins, W. I. Milne, and M. T. Cole, *Nano Converg.* **2**, 1 (2015).
- <sup>70</sup>S. R. Stock, “X-ray microtomography of materials,” *Int. Mater. Rev.* **44**, 141 (1999).
- <sup>71</sup>L. Vasarhelyi, Z. Konya, A. Kukovecz, and R. Vajtai, *Mater. Today Adv.* **8**, 100084 (2020).
- <sup>72</sup>K. Bavendiek, U. Ewert, A. Riedo, U. Heike and U. Zscherpel, in *Proceedings of the 18th World Conference on Nondestructive Testing*, Durban, 16–20 April 2012 (South African Institute for Non-Destructive Testing (SAINT), 2013), see <http://www.ndt.net/?id=12653>
- <sup>73</sup>O. Hemberg, M. Otendal, and H. M. Hertz, *Appl. Phys. Lett.* **83**, 1483–1485 (2003).
- <sup>74</sup>K. Dong, T. Zhang, M. Yu, Y. Wu, B. Zhu, F. Tan, S. Wang, Y. Yan, J. Yang, Y. Yang, F. Lu, G. Li, W. Fan, W. Hong, Z. Zhao, W. Zhou, L. Cao, and Y. Gu, *J. Appl. Phys.* **123**, 243301 (2018).
- <sup>75</sup>G. Geloni, V. Kocharyan, and E. Saldin, *J. Synchrotron Radiat.* **22**, 288–316 (2015).
- <sup>76</sup>R. Mokso, F. Marone, D. Habertür, J. C. Schittny, G. Mikuljan, A. Isenegger, and M. Stampanoni, *AIP Conf. Proc.* **1365**, 38–41 (2011).
- <sup>77</sup>M. Ge, D. S. Coburn, E. Nazaretski, W. Xu, K. Gofron, H. Xu, Z. Yin, and W.-K. Lee, *Appl. Phys. Lett.* **113**, 083109 (2018).
- <sup>78</sup>V. Cnudde and M. N. Boone, *Earth Sci. Rev.* **123**, 1–17 (2013).
- <sup>79</sup>C. Chang and A. Sakdinawat, *Nat. Commun.* **5**, 4243 (2014).
- <sup>80</sup>Z. Yu, J. Wang, and Y. Liu, *MRS Bull.* **45**, 283–289 (2020).
- <sup>81</sup>I. Mohacsi, I. Vartiainen, B. Rösner, M. G.-Sicairos, V. A. Guzenko, I. McNulty, R. Winarski, M. V. Holt, and C. David, *Sci. Rep.* **7**, 43624 (2017).

- <sup>82</sup>N. S. Hussein, D. P. Kumah, J. Z. Yi, C. J. Torbet, D. A. Arms, E. M. Dufresne, T. M. Pollock, J. Wayne Jones, and R. Clarke, *Acta Mater.* **56**, 4715–4723 (2008).
- <sup>83</sup>A. Lübcke, J. Braenzel, A. Dehlinger, M. Schnürer, H. Stiel, P. Guttman, S. Rehbein, G. Schneider, S. Werner, R. Kemmler, S. Ritter, M. Raugust, T. Wende, M. Behrendt, and M. Regehly, *Rev. Sci. Instrum.* **90**, 043111 (2019).
- <sup>84</sup>Z. Wang, J. Chen, and S. C. H. Hoi, *IEEE Trans. Pattern Anal. Mach. Intell.* **43**, 3365–3387 (2021).
- <sup>85</sup>Y. Sun, L. Li, P. Cong, Z. Wang, and X. Guo, *J. X-Ray Sci. Technol.* **25**, 857 (2017).
- <sup>86</sup>M. Bizhani, O. H. Ardakani, and E. Little, *Sci. Rep.* **12**, 4264 (2022).
- <sup>87</sup>D. Placko and I. Dufour, *IEEE Trans. Magn.* **29**, 3192–3194 (1993).
- <sup>88</sup>I. Dufour, D. Placko, and M. Geoffroy, *NDT & E Int.* **28**, 225–233 (1995).
- <sup>89</sup>H. Sun, R. Ali, M. Johnson, and J. R. Bowler, *AIP Conf. Proc.* **760**, 516–522 (2005).
- <sup>90</sup>D. M. Caetano, T. Rabuske, J. Fernandes, M. Pelkner, C. Fermon, S. Cardoso, B. Ribes, F. Franco, J. Paul, M. Piedade, and P. P. Freitas, *IEEE Trans. on Industrial Electronics* **66**, 7326 (2019).
- <sup>91</sup>T. Peng, J. Moulin, Y. L. Bihan, and F. Alves, in *Proceedings of the SPIE 8691, Nanosensors, Biosensors, and Info-Tech Sensors and Systems* (SPIE, 2013), p. 86910O.
- <sup>92</sup>K. Tsukada, H. Shobu, Y. Goda, T. Kobara, K. Sakai, T. Kiwa, and M. M. Saari, *IEEE Magn. Lett.* **10**, 1–5 (2019).
- <sup>93</sup>B. Wincheski, J. Simpson, J. P. Seebo, and J. Powell, *AIP Conf. Proc.* **1430**, 366–372 (2012).
- <sup>94</sup>R. C. Black and F. C. Wellstood, *Appl. Phys. Lett.* **64**, 100–102 (1994).
- <sup>95</sup>B. Hoffmann, R. Houbertz, and U. Hartmann, *Appl. Phys. A: Mater. Sci. Process.* **66**, S409–S413 (1998).
- <sup>96</sup>M. A. Lantz, S. P. Jarvis, and H. Tokumoto, *Appl. Phys. Lett.* **78**, 383–385 (2001).
- <sup>97</sup>M. R. Cherry, S. Sathish, J. Welter, R. Reibel, and M. P. Blodgett, *AIP Conf. Proc.* **1430**, 324–331 (2012).
- <sup>98</sup>M. Nakazawa, M. Tabaru, T. Takayasu, T. Aoyagi, and K. Nakamura, *Acoust. Sci. Technol.* **36**, 139–148 (2015).
- <sup>99</sup>C. Risser, H. J. Welsch, H. Fonfara, W. Bost, S. Weber, H. Hewener, and S. Tretbar, in *2015 IEEE International Ultrasonics Symposium (IUS)* (IEEE, 2015), pp. 1–4.
- <sup>100</sup>B. Wan, B. Hu, and X. Chen, *NDT&E Int.* **131**, 102693 (2022).
- <sup>101</sup>M. Lewandowski, M. Walczak, B. Witek, and T. Steifer, in *Proceedings of the 2016 IEEE International Ultrasonics Symposium (IUS)* (IEEE, 2016), pp. 1–4.
- <sup>102</sup>P. Després and X. Jia, *Phys. Med.* **42**, 76–92 (2017).